Bulgarian Chemical Communications, Volume 58, Issue 4 (pp. 492-503) 2026 *DOI: 10.34049/bcc.58.4.5756*

Integrated *in silico* discovery of anti-apoptotic sesquiterpenoid candidates from *Inula japonica* against hepatocarcinoma

H. D. Nguyen*

Faculty of Biology, Thai Nguyen University of Education, Thai Nguyen, 24124, Vietnam

Received: February 20, 2026; Revised: May 11, 2026

Hepatocellular carcinoma is a leading cause of cancer mortality, and resistance to programmed cell death remains a major barrier to durable therapeutic responses. Natural products from *Inula japonica*, particularly sesquiterpenoids, represent a chemically diverse source of anticancer scaffolds with potential to modulate anti-apoptotic signaling. An integrated *in silico* workflow evaluated nine reported sesquiterpenoids (CPD1-CPD9) against the anti-apoptotic target Myeloid Cell Leukemia 1 (Mcl-1) (PDB: 6B4U), using Simvastatin as a clinically used apoptosis-oriented comparative compound. Docking predicted consistently favorable affinities (-7.56 to -8.84 kcal/mol), with CPD9 (1-*O*-acetyl-6-*O*-isobutyrylbritannilactone) yielding the numerically most negative score among the screened sesquiterpenoids (-8.84 kcal/mol), which was essentially comparable to Simvastatin (-8.80 kcal/mol) and engaging the canonical groove largely through hydrophobic and van der Waals contacts. In 100 ns molecular dynamics simulations, both CPD9-6B4U and Simvastatin-6B4U complexes remained stable, while CPD9 showed comparatively reduced late-stage deviation and solvent exposure. MMGBSA (Molecular mechanics generalized Born surface area) analysis estimated stronger mean binding for Simvastatin than for CPD9, driven mainly by a more favorable van der Waals component. pkCSM profiling suggested improved modeled solubility and permeability for CPD9 but indicated an AMES-positive alert. DFT (Density Functional Theory) descriptors supported a harder, more electrophilic electronic profile for CPD9 relative to Simvastatin. These results nominate CPD9 a prioritized sesquiterpenoid scaffold for further optimization rather than a directly developable lead, particularly because its AMES-positive alert must be resolved before advancement.

Keywords: Anti-apoptosis; DFT; Hepatocarcinoma; Mcl-1; Molecular modeling; Sesquiterpenoids.

INTRODUCTION

Hepatocellular carcinoma (HCC) remains a major global health burden and one of the leading causes of cancer-related mortality [1]. Poor outcomes in advanced disease are partly driven by tumor adaptation to cytotoxic stress and impaired apoptosis regulation [2]. Among apoptosis-related pathways, anti-apoptotic B-cell lymphoma 2 (Bcl-2) family proteins promote survival by restraining mitochondrial outer membrane permeabilization through sequestration of pro-death BH3-only activators and effectors [3]. Myeloid cell leukemia 1 (Mcl-1) is a key pro-survival member of this family and has become an important target in BH3-mimetic discovery [4]. However, the physicochemical complexity of the Mcl-1 BH3-binding groove and safety-related concerns continue to complicate inhibitor development [5]. Recent studies further support Mcl-1 as a relevant but challenging anticancer target. In HCC models, dual inhibition of Mcl-1 and Bcl-2 using MIK665/S64315 and venetoclax synergistically induced intrinsic apoptotic cell death [6]. Other recent efforts, including first-in-human evaluation of AZD5991 and preclinical development of BRD-810, compound 26, and macrocyclic Mcl-1 inhibitors, highlight continued attempts to improve potency, selectivity, pharmacokinetics, and safety [7, 8]. Nevertheless, no Mcl-1 inhibitor has yet been approved for clinical use.

Natural products from medicinal plants provide structurally diverse scaffolds for modulating apoptosis-related targets [9]. *Inula japonica* (Asteraceae) is a source of sesquiterpenoids and sesquiterpene lactones with reported cytotoxic and apoptosis-associated activity against hepatocarcinoma cell lines, including HepG2 and SMMC-7721 [10, 11]. *In silico* workflows can accelerate early prioritization by integrating structure-based screening, conformational stability assessment in explicit solvent, end-point free-energy estimation, and developability-oriented profiling before resource-intensive experimentation. AutoDock-based docking has become a widely adopted approach for pose generation and interaction mapping. At the same time, molecular dynamics simulations with GROMACS enable time-resolved evaluation of binding-mode persistence under physiologically relevant conditions [12]. Complementary MMGBSA (Molecular mechanics generalised Born surface area) analysis supports comparative energetic ranking from ensemble

* To whom all correspondence should be sent:
E-mail*: hungnd@tnue.edu.vn*

© 2026 Bulgarian Academy of Sciences, Union of Chemists in Bulgaria

snapshots, and pkCSM provides rapid ADMET (Absorption, Distribution, Metabolism, Excretion, Toxicity) inference using graph-based molecular signatures [13, 14]. Quantum-chemical calculations with ORCA further inform electronic descriptors relevant to noncovalent recognition and reactivity trends at the lead-optimization stage [15]. Accordingly, this study evaluated reported sesquiterpenoids from *I. japonica* against Mcl-1 (PDB: 6B4U), using Simvastatin as a clinically used apoptosis-associated comparative compound to contextualize binding, stability, and developability within a unified computational approach.

MATERIALS AND METHODS

Structural preparation of selected ligands

The list of sesquiterpenoids possessing anti-cancer activity against the SMMC-7721 human hepatocarcinoma cell line was collected in the previous study [16]. For details, the selected ligands, including 1β-hydroxyalantolactone (CPD1), eupatolide (CPD2), deacetylovatifolin (CPD3), 2α-acetoxy-4β-hydroxy-pseudoguaia-11(13)-en-12,8α-olide (CPD4), deacetylbritanin (CPD5), 2α,6α-diacetoxy-4β-hydroxy-pseudoguaia-11(13)-en-12,8α-olide (CPD6), 6α-isovaleryloxy-4-oxo-4,5-seco-guaia-1(5),11(13)-dien-12,8β-olide (CPD7), 6-*O*-isobutyrylbritannilactone (CPD8), and 1-*O*-acetyl-6-*O*-isobutyrylbritannilactone (CPD9), have molecular formulas $C_{17}H_{22}O_4$, $C_{15}H_{20}O_3$, $C_{15}H_{20}O_4$, $C_{17}H_{24}O_5$, $C_{17}H_{24}O_6$, $C_{19}H_{26}O_7$, $C_{20}H_{28}O_5$, $C_{19}H_{28}O_5$, and $C_{21}H_{30}O_6$, with molecular weights of 290.1518, 248.1412, 264.1362, 308.1624, 324.1573, 366.1679, 348.1937, 336.1937, and 378.2042 Da, respectively. Simvastatin, with molecular formula $C_{25}H_{38}O_5$ and molecular weight of 418.2719 Da, was chosen as a comparative reference compound because of its clinical use and reported apoptosis-associated anticancer activity (Figure 1).

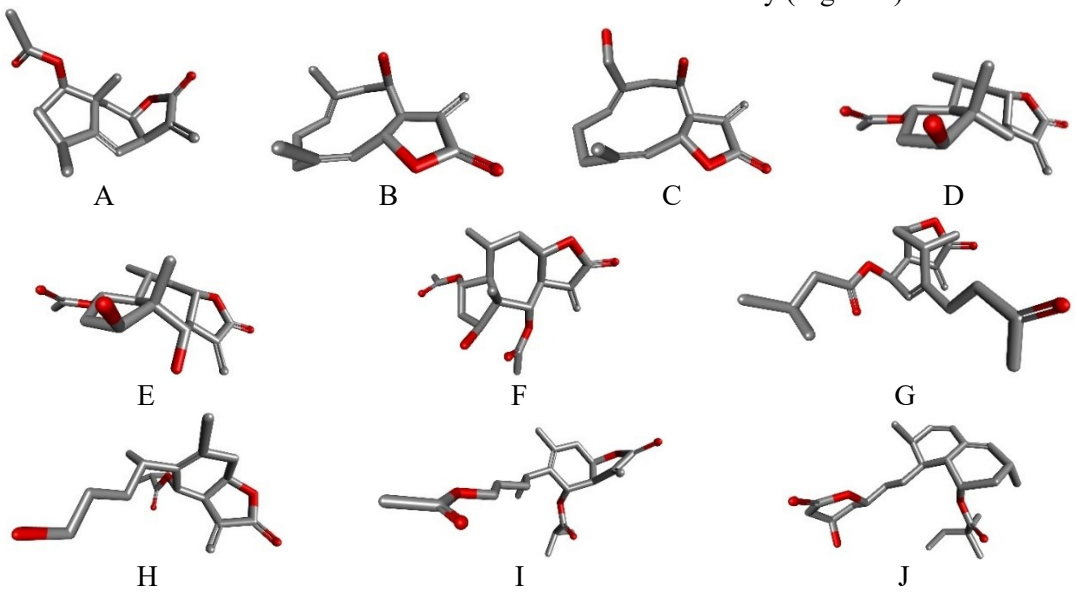


Figure 1. 3D Structures of selected ligands: (A) CPD1, (B) CPD2, (C) CPD3, (D) CDP4, (E) CPD5, (F) CPD6, (G) CPD7, (H) CPD8, (I) CPD9, and (J) Simvastatin.

Molecular docking analysis

Three-dimensional ligand conformations were prepared and exported in PDB format using BIOVIA Discovery Studio Visualizer. Polar hydrogen atoms were added, Gasteiger partial charges were assigned, and all rotatable torsions were defined as flexible. The structure of the anti-apoptotic target protein Mcl-1 (PDB: 6B4U) was obtained in PDB format from the RCSB Protein Data Bank [17]. Molecular docking was conducted with AutoDock Tools using a 60 × 60 × 60 grid box with a grid spacing of 0.375 Å. The docking region was centered at x = -2.774 Å, y = 16.913 Å, and z = 4.323 Å, following the binding-site coordinates reported for the 6B4U structure. The Lamarckian genetic algorithm guided conformational sampling and pose optimization to prioritize low-energy ligand-protein complexes with favorable intermolecular contacts. After docking, the highest-scoring binding mode was visualized and interpreted in Discovery Studio Client 2024, then evaluated against the docking profile of Simvastatin on the identical receptor as a reference standard to contextualize relative binding characteristics. Docking scores were interpreted as qualitative, within-protocol ranking metrics rather than quantitative measures of binding strength.

Molecular dynamics simulation

Molecular dynamics simulations were performed for the best-ranked docked complex with the 6B4U protein over 100 ns using GROMACS 2024.4 [18]. Before simulation, the protein model was curated in Swiss-PdbViewer to restore missing atoms and unresolved residues where applicable [19], while ligand parameters and topologies were generated with SwissParam [20]. The protein-ligand complex was solvated in a triclinic periodic box filled with Simple Point Charge (SPC) water and supplemented with 0.15 M NaCl to mimic physiological ionic strength and ensure overall charge neutrality. Energy relaxation was then carried out for 50,000 minimization steps to remove unfavorable contacts. Equilibration consisted of a 200 ps NVT (Number of particles, Volume, and Temperature) stage followed by a 200 ps NPT stage at 300 K and 1.0 bar. For each system, one 100-ns production run was executed using a 2-fs time step, and trajectory frames were recorded at 10 ps intervals. Simulation outputs were analyzed in Grace to extract core descriptors of structural stability and compactness, including root mean square deviation (RMSD), per-residue root mean square fluctuation (RMSF), radius of gyration (Rg), number of hydrogen bonds (Hbonds), and solvent-accessible surface area (SASA). Conformational stability of bound states was further examined by structural superposition in UCSF Chimera 1.13.3, aligning representative snapshots to evaluate whether ligand positioning within the active site remained consistent from 0 ns to 100 ns. Persistence of key contacts, including hydrogen bonding, van der Waals, and hydrophobic interactions, was inspected across the trajectory to characterize the durability and time-dependent evolution of ligand engagement throughout the 100 ns simulations.

Assay protocol for ADMET prediction

Early-stage ADMET profiling is integral to drug discovery because it can reveal pharmacokinetic liabilities and potential toxicities before costly downstream development, thereby reducing late-stage failures and facilitating the prioritization of compounds with more suitable developability. In the present work, the pkCSM web server was applied to predict ADMET-associated endpoints for CPD9 and Simvastatin. Using graph-based molecular signatures, pkCSM infers descriptors linked to absorption, distribution, metabolism, excretion, and toxicity, allowing a structured *in silico* comparison of these properties across the evaluated candidates.

Molecular mechanics generalized Born surface area (MMGBSA) analysis

Binding free energies for the CPD9-6B4U and Simvastatin-6B4U complexes were estimated using MMGBSA analysis implemented in gmx_MMPBSA under the CHARMM36 force field. In this framework, the generalized Born term was used to approximate the electrostatic contribution to solvation in an implicit solvent representation. In contrast, non-polar solvation was quantified from the solvent-accessible surface area. Energy components were extracted from the molecular dynamics trajectories using 125 uniformly distributed snapshots collected at 80 ps intervals over the 20-100 ns segment, corresponding to an 80 ns analysis window. Mean values derived from these frames were used to reflect within-trajectory temporal variability in ligand-protein coupling and to characterize relative MMGBSA energetic trends within the simulated environment. These endpoint estimates were interpreted as approximate within-protocol values rather than definitive experimental binding affinities or standalone criteria for lead superiority.

Quantum chemistry computation using the Density Functional Theory (DFT) method

Geometry optimization of CPD9 and Simvastatin was performed using the ORCA 6.1.0 quantum-chemistry suite. Molecular structures were first built in Avogadro and subsequently inspected, visualized, and subjected to orbital interpretation with IboView (v20211019). Density functional theory calculations were carried out at the B3LYP/6-31G(d,p) level to obtain reliable ground-state geometries and electronic-structure descriptions. Based on the optimized conformations, frontier orbital energies (HOMO and LUMO) were determined and used to estimate the energy gap (ΔE) and related reactivity descriptors, including chemical potential (μ), electronegativity (χ), hardness (η), softness (σ), and electrophilicity index (ω). These descriptors were derived through Koopmans-type relationships to support the comparative evaluation of the electronic characteristics of the investigated molecules [21, 22].

RESULTS AND DISCUSSION

Molecular docking analysis

Molecular docking supports structure-based screening by exploring ligand conformations and orientations inside a predefined binding pocket, followed by ranking with a scoring function that approximates binding propensity. Despite clear utility for prioritization, docking scores remain

model-dependent and sensitive to protein/ligand flexibility and parametrization; therefore, subsequent refinement by dynamics or end-point free-energy methods is commonly recommended [23]. Within apoptosis research, anti-apoptotic Bcl-2 family members are central regulators of mitochondrial cell-death control, and pharmacologic disruption of BH3-groove interactions has emerged as a validated anticancer strategy [24]. Before production docking, the protocol was validated by redocking the co-crystallized ligand and comparing the regenerated pose with the crystallographic conformation. This procedure yielded an RMSD of 0.9700 Å (Figure 2), indicating close pose reproduction. RMSD values below 2 Å are commonly used as a practical criterion for acceptable docking performance [25]. Following validation, candidate binding poses were ranked by docking score and the lowest-scoring conformations were selected for downstream interaction assessment.

The binding energies and key non-covalent contacts (hydrogen bonding, van der Waals, and hydrophobic interactions) observed between the docked ligands and the 6B4U protein were summarized in Table 1.

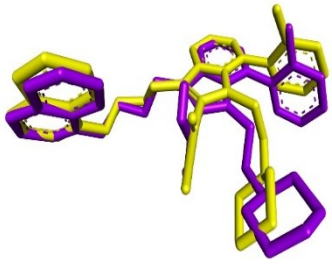


Figure 2. Superimposition of the docked and native ligands for validation of the molecular docking protocol on protein 6GL8 (violet = native, yellow = docked)

Table 1. Interactions between the docked ligands and the protein 6B4U.

Docked ligands	Binding energy (kcal/mol)	Hydrogen bond interaction	Van der Waals interaction	Hydrophobic interaction
CPD1	-8.20	-	Phe228, Met231, Leu235, Val249, Arg263, Thr266, Phe270	Met250, Val253, Phe254, Leu267
CPD2	-8.06	Leu246, Gly271	Leu235, Phe254, Ile294	Met231, Val249, Met250, Val253, Leu267, Phe270, Val274, Leu290
CPD3	-7.56	Leu267	Met231, Leu235, Ile237, Val249, Val253, Phe254, Thr266, Ile268, Gly271, Ile294	Leu246, Met250, Phe270, Val274, Leu290
CPD4	-8.73	-	Phe228, Leu235, Leu246, Phe254, Thr266, Val274, Leu290, Ile294	Met231, Val249, Met250, Val253, Leu267, Phe270
CPD5	-8.47	Leu267	Phe228, Leu235, Leu246, Val249, Phe254, Arg263, Thr266, Gly271, Val274, Leu290, Ile294	Met231, Met250, Val253, Leu267, Phe270
CPD6	-8.24	-	Ala227, Phe228, Leu235, Leu246, Phe254, Thr266, Gly271, Val274, Leu290, Ile294	Met231, Val249, Met250, Val253, Phe270
CPD7	-8.69	Met250	Ala227, Phe228, Met231, Leu235, Val249, Phe254, Thr266, Gly271, Val274, Leu290, Ile294	Leu246, Met250, Val253, Leu263, Phe270
CPD8	-8.35	Leu246, Leu267	Phe228, Leu235, Phe254, Arg263, Thr266	Ala227, Met231, Val249, Met250, Val253, Leu267, Phe270
CPD9	-8.84	-	Phe228, Met231, Leu235, Ile237, Leu246, Val253, Phe254, Arg263, Thr266, Gly271, Val274, Leu290, Ile294	Val249, Met250, Leu267, Phe270
Simvastatin	-8.80	Leu246	Ala227, Thr266, Ile294	Phe228, Met231, Leu235, Val249, Met250, Val253, Phe254, Arg263, Leu267, Phe270

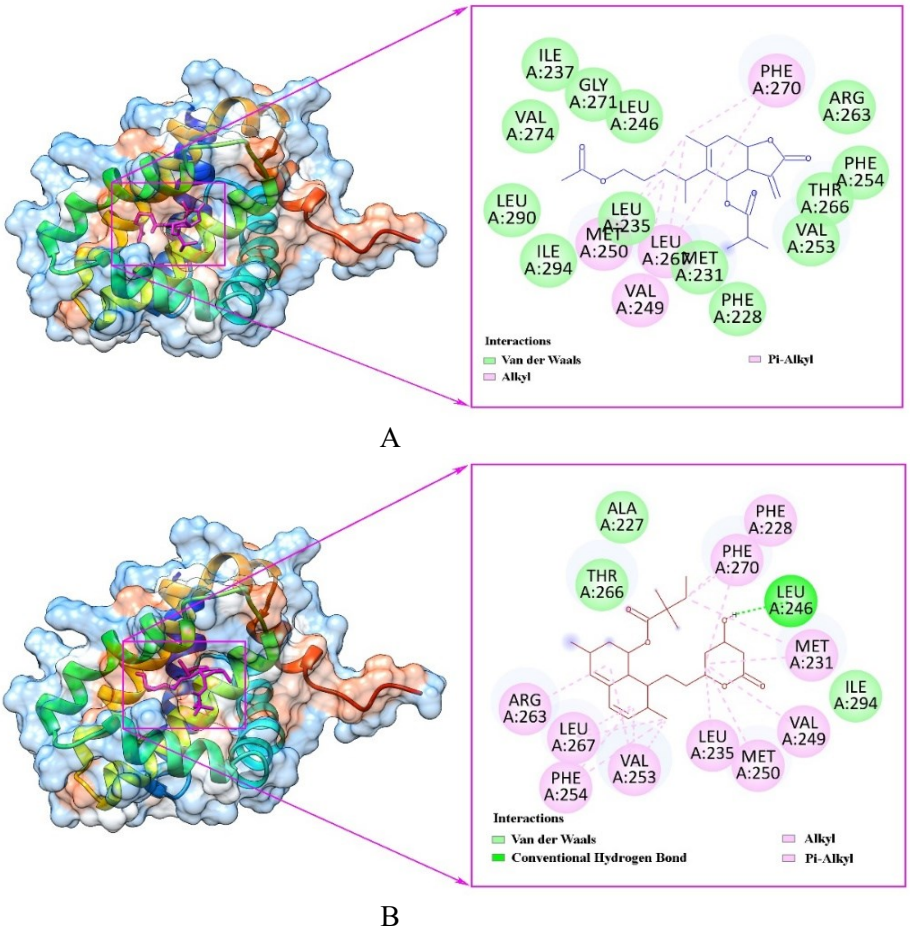


Figure 3. Molecular docking model and 2D interaction diagram of CPD9 (A) and Simvastatin (B) with 6B4U protein

Docking of CPD1-CPD9 against the 6B4U target indicated consistently favorable predicted affinities (-7.56 to -8.84 kcal/mol), with CPD9 presenting the most negative binding energy (-8.84 kcal/mol), which was essentially comparable to that of Simvastatin (-8.80 kcal/mol) rather than meaningfully superior. Because the difference between CPD9 and Simvastatin was only 0.04 kcal/mol, this small numerical gap was not interpreted as evidence of stronger binding. Instead, docking was used as a qualitative prioritization step based on score ranking, binding-site occupancy, and interaction patterns. Among the screened ligands, CPD9 occupied the canonical groove region delineated by Met250, Val253, Arg263, Thr266, Leu267, Phe270, and Gly271, indicating a well-positioned docking pose within a residue cluster repeatedly implicated in BH3-groove recognition and inhibitor optimization for MCL-1-like pockets (Figure 3A) [26]. Notably, CPD9 formed no hydrogen bond in the docking pose, suggesting that stabilization is dominated by close-range packing and non-directional contacts rather than a single polar anchor. A broad van der Waals network was predicted for CPD9, involving Phe228, Met231, Leu235, Ile237, Leu246, Val253, Phe254, Arg263, Thr266, Gly271, Val274, Leu290, and Ile294, accompanied by hydrophobic contacts with Val249, Met250, Leu267, and Phe270. The prevalence of hydrophobic and dispersion-driven interactions aligns with physical descriptions of protein-ligand stabilization in apolar grooves, where surface complementarity and burial of nonpolar areas can compensate for limited hydrogen bonding [27].

Simvastatin, used as a reference ligand, displayed a partially overlapping interaction footprint, with active-site involvement of Ala227, Met250, Val253, Arg263, Thr266, and Leu267 and a hydrogen bond to Leu246. Hydrophobic contacts spanned Phe228, Met231, Leu235, Val249, Met250, Val253, Phe254, Arg263, Leu267, and Phe270, while van der Waals contributions were noted for Ala227, Thr266, and Ile294. The overlap between CPD9 and Simvastatin at Leu246, Met250, Val253, Thr266, Leu267, Phe270 supports occupation of the same predicted pocket region, strengthening qualitative comparability of the docking poses across both systems (Figure 3B). In addition, Simvastatin has documented pleiotropic anticancer-relevant mechanisms in the literature, including modulation of apoptosis-related pathways, supporting suitability

as a benchmark compound in an anti-apoptosis-oriented computational workflow [28].

Across the remaining candidates, CPD4 (-8.73) and CPD7 (-8.69) also approached the reference score, whereas CPD3 showed the least favorable value (-7.56). Several ligands exhibited one or more hydrogen bonds (CPD2: Leu246 and Gly271; CPD3: Leu267; CPD5: Leu267; CPD7: Met250; CPD8: Leu246 and Leu267), yet the most negative docking score was associated with CPD9 in the absence of hydrogen bonding, reinforcing the possibility that pocket-filling hydrophobic, van der Waals complementarity can dominate predicted affinity in this binding site [29].

Based on the docking rank order among the screened sesquiterpenoids and the extensive, pocket-spanning contact pattern that substantially overlaps the Simvastatin interaction region, CPD9 represents the most justified choice for molecular dynamics simulations and downstream energetic validation, with Simvastatin retained as the comparator for stability and binding persistence analyses. This prioritization is consistent with contemporary guidance that docking-based triage benefits from follow-up sampling to assess conformational adaptation and interaction durability, particularly in Bcl-2 family grooves, where induced fit and contact reorganization can influence final rankings.

Molecular dynamics simulation

Molecular dynamics (MD) simulations were used to evaluate the time-dependent behavior of the CPD9-6B4U and Simvastatin-6B4U complexes in explicit solvent. Trajectory descriptors, including RMSD, RMSF, Rg, hydrogen bonds, and SASA, were analyzed to assess global stability, local flexibility, compactness, polar contacts, and solvent exposure [30]. Therefore, the evaluation systematically investigated these metrics to determine the stability, flexibility, and solvent exposure of the CPD9-6B4U and Simvastatin-6B4U complexes throughout the simulation timeframe.

Across 100 ns, backbone RMSD traces for the CPD9-6B4U and Simvastatin-6B4U complexes remained within a narrow sub-nanometer band, supporting preservation of the overall fold without a sustained deviation pattern compatible with large-scale destabilization [31].

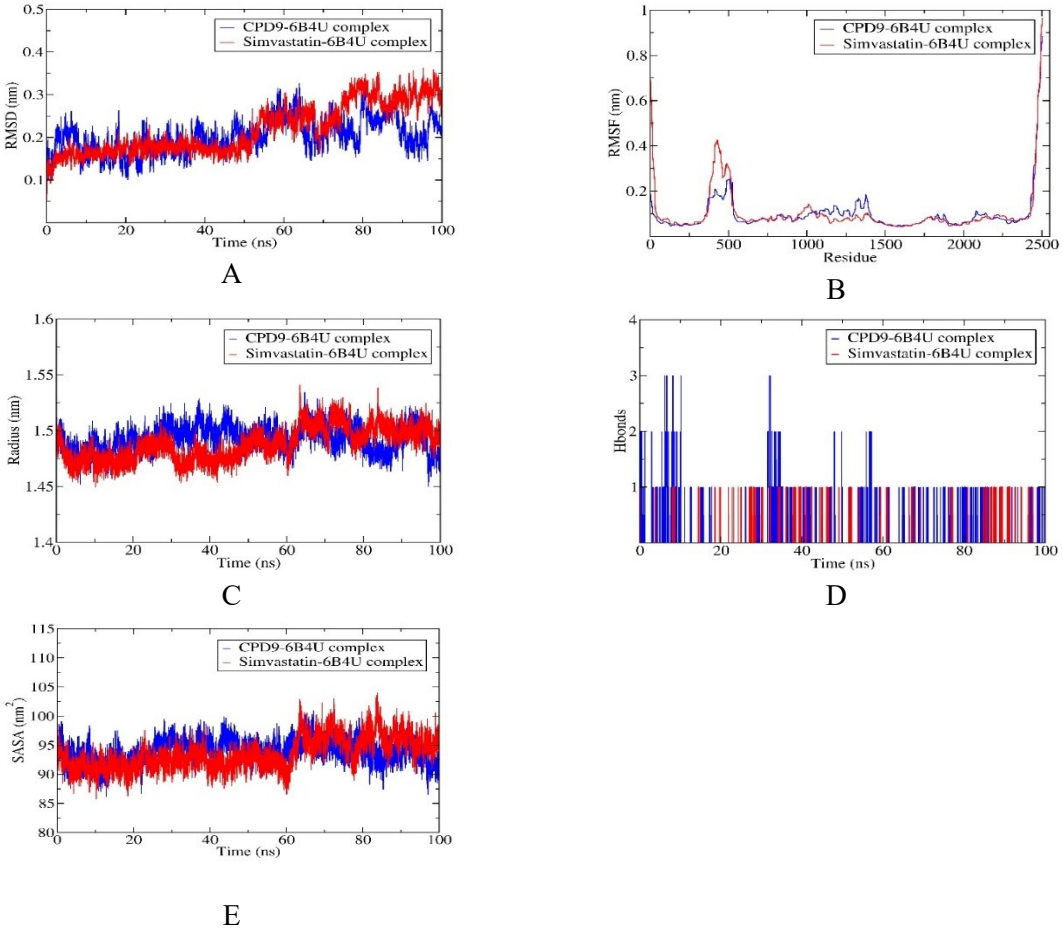


Figure 4. Results of MD simulation for the bindings of CPD9 (blue) and Simvastatin (red) with 6B4U protein: (A) RMSD, (B) RMSF, (C) Rg, (D) Hbonds, (E) SASA

After early equilibration and a modest increase around 50-70 ns, the Simvastatin-6B4U trajectory more frequently occupied a higher RMSD envelope after 70 ns, whereas CPD9-6B4U showed a lower late-stage deviation trend (Figure 4A).

Residue-level RMSF analysis over the Ser171-Glu325 segment showed low fluctuations for both complexes, with no sharp peaks or localized destabilization events (Figure 4B). Minor trace differences were observed, suggesting only subtle trajectory-level variation in local flexibility.

Rg profiles also showed broadly overlapping ranges, indicating comparable global compactness. However, Simvastatin-6B4U displayed a mild tendency toward higher Rg values after 60 ns, while CPD9-6B4U maintained a slightly tighter late-stage distribution (Figure 4C). Because Rg tracks mass distribution around the center of geometry, these patterns support a more expanded conformational ensemble for the Simvastatin-bound state in the late stage, alongside a comparatively compact ensemble under CPD9 [32].

Hydrogen-bond analysis showed sparse polar contacts in both complexes, with counts mostly fluctuating around 0-1. CPD9-6B4U displayed occasional short-lived spikes above 1, especially early in the trajectory, whereas Simvastatin-6B4U largely remained within the 0-1 range (Figure 4D). These transient changes likely reflect local rearrangements, water mediation, and side-chain reorientation rather than persistent polar anchoring [33].

SASA profiles further supported the late-stage differences between the two systems. Before 60 ns, both complexes overlapped mainly within the low-to-mid 90 nm^2 region. After 60 ns, Simvastatin-6B4U sampled higher SASA values more frequently and showed broader fluctuations, consistent with increased surface exposure and pocket-breathing behavior (Figure 4E). In contrast, CPD9-6B4U remained within a somewhat lower SASA band toward the end of the run, suggesting reduced solvent exposure in the final segment [34].

Overall, both complexes remained stable across the 100 ns trajectories. CPD9-6B4U showed a descriptive late-stage trend toward lower RMSD, slightly tighter compactness, and reduced solvent exposure, whereas Simvastatin-6B4U displayed modestly higher RMSD, Rg, and SASA variability after mid-simulation. These MD results were interpreted as single-trajectory descriptive observations supporting further energetic analysis, rather than as replicate-based statistical evidence of superior stability.

Free binding energy (MMGBSA) analysis

Molecular mechanics generalized Born surface area (MMGBSA) was used as an endpoint approach to estimate relative binding energetics from MD snapshots, complementing docking by incorporating conformational and implicit-solvent effects. In gmx_MMPBSA, the total binding estimate was decomposed into gas-phase interactions (ΔG_GAS = ΔVDW + ΔEEL) and solvation terms (ΔG_SOLV = ΔE_GB + ΔE_SURF), where ΔE_GB represents polar solvation and ΔE_SURF reflects nonpolar surface-area contributions [35]. As summarized in Table 2, both complexes displayed favorable mean MMGBSA totals, with Simvastatin-6B4U showing a more negative ΔTOTAL (-28.70 ± 2.35 kcal/mol) than CPD9-6B4U (-17.59 ± 3.59 kcal/mol), indicating a stronger MMGBSA-estimated binding profile for Simvastatin under the same protocol and sampling window. Accordingly, the MMGBSA result does not support interpreting CPD9 as the stronger-binding ligand relative to Simvastatin. Instead, it identifies binding-energy optimization, particularly improvement of van der Waals stabilization, as a key requirement for CPD9. The energetic difference was dominated by dispersion-driven packing: ΔVDW was substantially more favorable for Simvastatin (-37.01 ± 2.56 kcal/mol) than for CPD9 (-22.06 ± 3.42 kcal/mol), consistent with MMGBSA observations that hydrophobic shape complementarity and van der Waals contacts often contribute strongly to binding in apolar grooves. Electrostatics contributed modestly for both systems (ΔEEL = -3.01 ± 6.80 kcal/mol for Simvastatin; -3.85 ± 6.88 kcal/mol for CPD9), while polar solvation opposed complex formation more strongly for Simvastatin (ΔEGB = 15.94 ± 6.89 kcal/mol) than for CPD9 (11.44 ± 6.55 kcal/mol). Nonpolar solvation favored binding in both cases (ΔE_SURF = -4.61 ± 0.31 kcal/mol for Simvastatin; -3.12 ± 0.49 kcal/mol for CPD9), partially offsetting the generalized Born penalty and reinforcing a binding mode enriched in nonpolar burial [36].

Aggregated terms confirmed the same trend. Simvastatin showed more favorable gas-phase energy (ΔG_GAS = -40.02 ± 7.43 kcal/mol) than CPD9 (-25.91 ± 8.35 kcal/mol), whereas solvation opposed binding more strongly for Simvastatin (ΔG_SOLV = 11.33 ± 6.77 kcal/mol) than CPD9 (8.32 ± 6.34 kcal/mol). The smaller ΔTOTAL standard deviation for Simvastatin also suggests more consistent binding energetics across the analyzed snapshots compared with CPD9 [37].

Taken together, MMGBSA decomposition indicates that Simvastatin-6B4U achieves a stronger mean binding estimate primarily through enhanced

van der Waals stabilization and slightly more favorable nonpolar solvation, despite a larger polar-solvation penalty. CPD9-6B4U shows weaker overall MMGBSA favorability but benefits from a smaller generalized Born penalty and marginally more favorable electrostatics. Therefore, CPD9 was not interpreted as superior to Simvastatin in terms of MMGBSA binding energetics. Rather, CPD9 was retained as a prioritized sesquiterpenoid scaffold because it showed the most favorable docking score among the screened sesquiterpenoids, maintained acceptable single-trajectory MD behavior, and displayed several developability-relevant features in ADMET and DFT analyses. The less favorable ΔTOTAL and ΔVDW values of CPD9 are now explicitly treated as limitations and as targets for future structure-guided optimization.

ADMET prediction analysis

In silico ADMET profiling was conducted to contextualize developability-relevant pharmacokinetic behavior and safety flags for CPD9, compared with Simvastatin, using the pkCSM framework, which relies on graph-based molecular signatures for multi-endpoint prediction. Table 3 compiles the predicted absorption, distribution, metabolism, excretion, and toxicity outputs and enables an early-stage comparison of liabilities and strengths across both candidates within a consistent descriptor model.

Table 2. Free energy of binding obtained using MMGBSA calculations.

Energy component	Average (kcal/mol)		Standard deviation	
	CPD9-6B4U	Simvastatin-6B4U	CPD9-6B4U	Simvastatin-6B4U
ΔVDWAALS	-22.06	-37.01	3.42	2.56
ΔEEL	-3.85	-3.01	6.88	6.80
ΔEGB	11.44	15.94	6.55	6.89
ΔESURF	-3.12	-4.61	0.49	0.31
ΔGGAS	-25.91	-40.02	8.35	7.43
ΔGSOLV	8.32	11.33	6.34	6.77
ΔTOTAL	-17.59	-28.70	3.59	2.35

Table 3. Predicted ADMET properties of CPD9 and Simvastatin

ADMET properties	Unit	CPD9	Simvastatin
Water solubility	(Log mol/L)	-3.967	-5.239
Caco2 permeability	(Log Papp in 10^{-6} cm/s)	1.42	1.106
Intestinal absorption (Human)	(% Absorbed)	100	96.822
Skin permeability	(Log Kp)	-3.054	-3.547
P-glycoprotein substrate	Yes/No	No	Yes
P-glycoprotein I inhibitor	Yes/No	Yes	Yes
P-glycoprotein II inhibitor	Yes/No	No	Yes
VDss (Volume of distribution at steady state)	(Log L/kg)	-0.203	0.328
Fraction unbound (human)	(Fu)	0.198	0.196
BBB (Blood brain barrier) permeability	(Log BB)	-0.666	-0.304
CNS (Central nervous system) permeability	(Log PS)	-2.846	-2.262
CYP2D6 substrate	Yes/No	No	No
CYP3A4 substrate	Yes/No	Yes	Yes
CYP1A2 inhibitor	Yes/No	No	No
CYP2C19 inhibitor	Yes/No	No	No
CYP2C9 inhibitor	Yes/No	No	No
CYP2D6 inhibitor	Yes/No	No	No
CYP3A4 inhibitor	Yes/No	No	No
Total clearance	(Log ml/min/kg)	1.325	0.775
Renal OCT2 (Organic cation transporter 2) substrate	Yes/No	Yes	No
AMES toxicity	Yes/No	Yes	No
Maximum tolerated dose (human)	(Log mg/kg/day)	0.278	-0.164
Human Ether-a-go-go Related Gene (hERG) I inhibitor	Yes/No	No	No
hERG II inhibitor	Yes/No	No	Yes
Oral rat acute toxicity (LD50)	(mol/kg)	2.181	2.302
Oral rat chronic toxicity (LOAEL)	(Log mg/kg_bw/day)	1.812	1.251
Hepatotoxicity	Yes/No	No	No
Skin sensation	Yes/No	No	No
Tetrahymena pyriformis toxicity	(Log ug/L)	0.485	0.877
Minnow toxicity	(Log mM)	0.999	-0.215

Predicted aqueous solubility was higher for CPD9 than for Simvastatin (-3.967 *vs*. -5.239 log mol/L), suggesting a less pronounced solubility limitation for CPD9. Absorption-related descriptors also favored CPD9, including higher Caco-2 permeability (1.42 *vs*. 1.106 log Papp) and slightly higher intestinal absorption (100% *vs.* 96.822%) [38]. CPD9 was not predicted as a P-glycoprotein substrate, whereas Simvastatin was; however, both compounds were predicted as P-glycoprotein I inhibitors, and only Simvastatin was predicted as a P-glycoprotein II inhibitor [39].

Distribution descriptors showed higher VDss for Simvastatin than CPD9 (0.328 *vs*. -0.203 log L/kg), while fraction unbound values were nearly identical (0.198 *vs*. 0.196). Both compounds showed negative central distribution indices, although Simvastatin had less negative logBB and logPS values, suggesting relatively higher modeled CNS access than CPD9 within the same prediction scale [40]. For metabolism, both compounds were predicted as CYP3A4 substrates and CYP2D6 non-substrates. No inhibition was predicted for CYP1A2, CYP2C19, CYP2C9, CYP2D6, or CYP3A4, suggesting limited CYP inhibition-related interaction risk in this model [41]. CPD9 showed higher predicted total clearance than Simvastatin (1.325 *vs.* 0.775 log ml/min/kg) and was annotated as an OCT2 substrate, whereas Simvastatin was not. This indicates a possible renal transporter-related liability for CPD9 [42]. Safety predictions revealed the most important limitation of CPD9: it was AMES-positive, while Simvastatin was AMES-negative. Neither compound was predicted as an hERG I inhibitor, but Simvastatin was predicted as an hERG II inhibitor, unlike CPD9 [43]. Acute and chronic rodent toxicity values were broadly comparable, and both compounds were predicted negative for hepatotoxicity and skin sensitization. Ecotoxicity endpoints differed numerically, but these values were not extrapolated beyond the model outputs [44]. Both values exceed the toxicity threshold (> -0.5), indicating a positive flag for this endpoint in both candidates. Neither compound meets the high acute toxicity criterion (logLC50 < -0.3). This result was not treated as a minor toxicity flag, because an AMES-positive alert indicates potential mutagenic/genotoxic liability and can substantially limit the direct developability of a candidate compound. Although this in silico prediction does not confirm experimental genotoxicity, it identifies CPD9 as a scaffold requiring careful structural optimization before further advancement. Therefore, the favorable predicted absorption, Caco-2 permeability, solubility, and non-P-gp-substrate profile of CPD9 should be interpreted cautiously and cannot compensate for the predicted genotoxicity liability. Future work should prioritize removal or reduction of the structural features responsible for the AMES-positive alert, followed by experimental AMES testing and complementary genotoxicity assays.

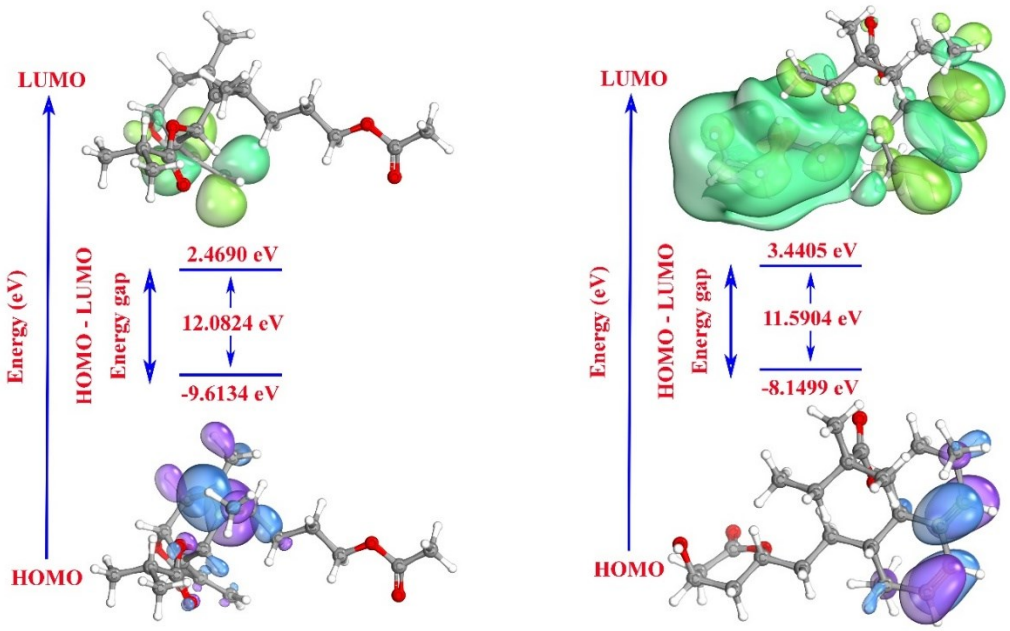
Collectively, pkCSM outputs suggest that CPD9 combines improved predicted solubility, permeability, and intestinal absorption with higher predicted clearance and an OCT2-substrate annotation. At the same time, Simvastatin shows stronger modeled tissue distribution and comparatively higher central distribution indices, along with an hERG II inhibition flag. The principal developability concern for CPD9 in this panel is the AMES-positive prediction, which typically warrants prioritization of confirmatory genotoxicity assessment or structural refinement during lead optimization.

Quantum chemistry computation using the DFT method

Density functional theory (DFT) descriptors were examined for CPD9 and Simvastatin to compare frontier-orbital characteristics and global conceptual-DFT reactivity indices derived from electronic structure analysis. Frontier orbital energies provide a compact proxy for charge-transfer tendencies, where lower EHOMO generally reflects reduced electron-donor propensity and lower ELUMO is commonly associated with enhanced electron-acceptor character within the same computational level [45]. As shown in Table 4, CPD9 exhibits a deeper EHOMO (-9.6134 eV) than Simvastatin (-8.1499 eV), consistent with CPD9's higher resistance to electron removal under the applied model. CPD9 also presents a lower ELUMO (2.4690 eV) than Simvastatin (3.4405 eV), indicating comparatively stronger electron-acceptor character for CPD9 in the same descriptor space.

Table 4. Quantum descriptors of CPD9 and Simvastatin. EHOMO: highest occupied molecular orbitals; ELUMO: lowest unoccupied molecular orbitals; ΔE: energy gap; μ: chemical potential; χ: electronegativity; η: hardness; σ: softness; ω: electrophilicity index.

Molecule	EHOMO (eV)	ELUMO (eV)	ΔE (eV)	μ (eV)	χ (eV)	η (eV)	σ (eV^{-1})	ω (eV)
CPD9	-9.6134	2.4690	12.0824	-3.5722	3.5722	6.0412	0.1655	1.0561
Simvastatin	-8.1499	3.4405	11.5904	-2.3547	2.3547	5.7952	0.1726	0.4784



A B

Figure 5. HOMO and LUMO surface diagrams of CPD9 (A) and Simvastatin (B)

The HOMO-LUMO gap (ΔE) is frequently used as a qualitative indicator of electronic responsiveness and kinetic stability, with larger gaps often aligning with greater global hardness [46]. CPD9 shows a slightly larger ΔE (12.0824 eV) than Simvastatin (11.5904 eV), suggesting modestly higher electronic rigidity for CPD9 (Figure 5). This trend agrees with the conceptual descriptors hardness (η) and softness (σ): CPD9 has higher η (6.0412 eV) and lower σ (0.1655 eV^{-1}) than Simvastatin (η = 5.7952 eV; σ = 0.1726 eV^{-1}), supporting a shift toward a globally harder profile for CPD9.

Charge-transfer descriptors further differentiate the molecules. Chemical potential (μ) and electronegativity (χ) are commonly interpreted as global measures of electron-escaping tendency and electron-attracting character, respectively, within conceptual DFT [47]. CPD9 displays a more negative μ (-3.5722 eV) and higher χ (3.5722 eV) than Simvastatin (μ = -2.3547 eV; χ = 2.3547 eV), consistent with a stronger overall electron-attracting character for CPD9 in this framework. The electrophilicity index (ω), a global descriptor derived from μ and η and often used to summarize electrophile strength, is higher for CPD9 (1.0561 eV) than for Simvastatin (0.4784 eV), indicating greater predicted electrophilic character for CPD9 under the same assumptions used to compute global indices from frontier-orbital energies [48].

Overall, the descriptor pattern supports an electronic profile for CPD9 characterized by deeper frontier orbital energies, a slightly larger gap, increased global hardness, and higher electrophilicity relative to Simvastatin. Such trends are frequently discussed as contributors to differential noncovalent recognition and stabilization propensities in biomolecular environments, yet remain dependent on the chosen functional/basis set and the approximations used to map orbital energies to conceptual descriptors.

CONCLUSION

This study presents an integrated *in silico* evaluation of sesquiterpenoids from *I. japonica* against the anti-apoptotic protein Mcl-1 (6B4U) in hepatocarcinoma. CPD9 showed the numerically most negative docking score among the screened sesquiterpenoids (-8.84 kcal/mol), which was essentially comparable to that of Simvastatin (-8.80 kcal/mol), fitting deeply into the canonical groove *via* large van der Waals and hydrophobic contacts. Over 100 ns MD, both complexes remained stable, while CPD9 showed tighter late-stage behavior (lower backbone deviation, less Rg/SASA drift) than Simvastatin. MMGBSA, however, favored Simvastatin overall (ΔTOTAL -28.70 ± 2.35 kcal/mol) over CPD9 (-17.59 ± 3.59 kcal/mol), mainly due to stronger van der Waals stabilization (-37.01 *vs.* -22.06 kcal/mol). Thus, CPD9 should not be interpreted as the stronger-binding ligand based on MMGBSA. Instead, its weaker ΔTOTAL and ΔVDW values highlight the need for structure-guided optimization to improve pocket packing and dispersion-driven stabilization. ADMET predictions suggested that CPD9 has better modeled solubility

and permeability and is not a P-gp substrate, but it carries a key concern with an AMES-positive flag. DFT descriptors further indicated that CPD9 is electronically harder and more electrophilic than Simvastatin. Overall, CPD9 remains a prioritized sesquiterpenoid scaffold for further optimization, but not a directly developable lead in its current form, because its weaker MMGBSA binding estimate and major AMES-positive genotoxicity liability must be addressed.

Despite these computational signals, experimental validation is required to confirm true target engagement and anti-cancer efficacy. Future work should prioritize biochemical binding assays, hepatocarcinoma cell assays (apoptosis/viability and mitochondrial-pathway markers), and confirmatory genotoxicity testing to resolve the AMES-positive prediction, alongside transporter studies (OCT2) and broader safety profiling. Structure-guided refinement should aim to strengthen binding energy while reducing predicted liabilities. If CPD9 sustains potency and safety in preclinical tests, it could justify progression toward translational development for Mcl-1-driven hepatocarcinoma.

REFERENCES

1. F. Bray, M. Laversanne, H. Sung, J. Ferlay, R. L. Siegel, I. Soerjomataram, A. Jemal, *CA. Cancer J. Clin.*, **74**, 229 (2024).
2. J. U. Marquardt, F. Edlich, *Front. Oncol.*, **9**, 1421 (2019).
3. D. Kaloni, S. T. Diepstraten, A. Strasser, G. L. Kelly, *Apoptosis*, **28**, 20 (2023).
4. V. V Senichkin, A. Y. Streletskaia, A. S. Gorbunova, B. Zhivotovsky, G. S. Kopeina, *Cell Death Differ.*, **27**, 405 (2020).
5. S. I. Tantawy, N. Timofeeva, A. Sarkar, V. Gandhi, *Front. Oncol.*, **13**, 1226289 (2023).
6. M. Michalski, M. Bauer, F. Walz, D. Tümen, P. Heumann, P. Stöckert, M. Gunckel, C. Kunst, A. Kandulski, S. Schmid, M. Müller, K. Gülow, *Biomedicines*, **11**, 1666 (2023).
7. P. Desai, S. Lonial, A. Cashen, M. Kamdar, I. Flinn, S. O'Brien, J. S. Garcia, N. Korde, J. Moslehi, M. Wey, P. Cheung, S. Sharma, D. Olabode, H. Chen, F. Ali Syed, M. Liu, J. Saeh, M. Andrade-Campos, T. M. Kadia, J. S. Blachly, *Clin. Cancer Res.*, **30**, 4844 (2024).
8. U. Rauh, G. Wei, M. Serrano-Wu, G. Kosmidis, S. Kaulfuss, F. Siegel, K. Thede, J. McFarland, C. T. Lemke, N. Werbeck, K. Nowak-Reppel, S. Pilari, S. Menz, M. Ocker, W. Zhang, K. Davis, G. Poncet-Montange, J. Roth, D. Daniels, V. K. Kaushik, B. Hubbard, K. Ziegelbauer, T. R. Golub, *Nat. Cancer*, **5**, 1479 (2024).
9. P. Dhyani, P. Sati, E. Sharma, D. C. Attri, A. Bahukhandi, B. Tynybekov, A. Szopa, J. Sharifi-Rad, D. Calina, H. A. R. Suleria, W. C. Cho, *Cancer Cell Int.*, **22**, 305 (2022).
10. T. Wang, T. Chen, Q. Zhang, Y. Cheng, C. Xie, Q. Zhang, Y. Ding, *Chem. Biodivers.*, **20**, e202300220 (2023).
11. Y. Ding, T. Wang, T. Chen, C. Xie, Q. Zhang, *Bioorg. Chem.*, **101**, 103973 (2020).
12. S. Forli, R. Huey, M. E. Pique, M. F. Sanner, D. S. Goodsell, A. J. Olson, *Nat. Protoc.*, **11**, 905 (2016).
13. M. S. Valdés-Tresanco, M. E. Valdés-Tresanco, P. A. Valiente, E. Moreno, *J. Chem. Theory Comput.*, **17**, 6281 (2021).
14. D. E. Pires, T. L. Blundell, D. B. Ascher, *J. Med. Chem.*, **58**, 4066 (2015).
15. F. Neese, *WIREs Comput. Mol. Sci.*, **15**, e70019 (2025).
16. X. D. Wu, L. F. Ding, W. C. Tu, H. Yang, J. Su, L. Y. Peng, Y. Li, Q. S. Zhao, *Phytochemistry*, **129**, 68 (2016).
17. M. Bruncko, L. Wang, G. S. Sheppard, D. C. Phillips, S. K. Tahir, J. Xue, S. Erickson, S. Fidanze, E. Fry, L. Hasvold, G. J. Jenkins, S. Jin, R. A. Judge, P. J. Kovar, D. Madar, P. Nimmer, C. Park, A. M. Petros, S. H. Rosenberg, M. L. Smith, X. Song, C. Sun, Z.-F. Tao, X. Wang, Y. Xiao, H. Zhang, C. Tse, J. D. Leverson, S. W. Elmore, A. J. Souers, *J. Med. Chem.*, **58**, 4089 (2015).
18. D. Van Der Spoel, E. Lindahl, B. Hess, G. Groenhof, A. E. Mark, H. J. C. Berendsen, *J. Comput. Chem.*, **26**, 1701 (2005).
19. N. Guex, M. C. Peitsch, *Electrophoresis*, **18**, 2714 (1997).
20. V. Zoete, M. A. Cuendet, A. Grosdidier, O. Michielin, *J. Comput. Chem.*, **32**, 2359 (2011).
21. J. Luo, Z. Q. Xue, W. M. Liu, J. L. Wu, Z. Q. Yang, *J. Phys. Chem. A*, **110**, 12005 (2006).
22. R. Das, J. L. Vigneresse, P. K. Chattaraj, *Int. J. Quantum Chem.*, **114**, 1421 (2014).
23. P. C. Agu, C. A. Afiukwa, O. U. Orji, E. M. Ezeh, I. H. Ofoke, C. O. Ogbu, E. I. Ugwuja, P. M. Aja, *Sci. Rep.*, **13**, 13398 (2023).
24. C. M. Croce, D. Vaux, A. Strasser, J. T. Opferman, P. E. Czabotar, S. W. Fesik, *Cell Death Differ.*, **32**, 1369 (2025).
25. H. Gohlke, M. Hendlich, G. Klebe, *J. Mol. Biol.*, **295**, 337 (2000).
26. A. Bolomsky, M. Vogler, M. C. Köse, C. A. Heckman, G. Ehx, H. Ludwig, J. Caers, *J. Hematol. Oncol.*, **13**, 173 (2020).
27. G. G. Ferenczy, M. Kellermayer, *Comput. Struct. Biotechnol. J.*, **20**, 1946 (2022).
28. C. Liu, H. Chen, B. Hu, J. Shi, Y. Chen, K. Huang, *Front. Pharmacol.*, **14**, 1188926 (2023).
29. R. Meli, G. M. Morris, P. C. Biggin, *Front. Bioinforma.*, **2**, 885983 (2022).
30. O. M. H. Salo-Ahen, I. Alanko, R. Bhadane, A. M. J. J. Bonvin, R. V Honorato, S. Hossain, A. H. Juffer, A. Kabedev, M. Lahtela-Kakkonen, A. S. Larsen, E. Lescrinier, P. Marimuthu, M. U. Mirza, G. Mustafa, A. Nunes-Alves, T. Pantsar, A. Saadabadi, K. Singaravelu, M. Vanmeert, *Processes*, **9**, 71 (2021).
31. R. Shukla, T. Tripathi, D. B. Singh, ed., Springer

Singapore, 2020, p. 133.
32. M. Y. Lobanov, N. S. Bogatyreva, O. V Galzitskaya, *Mol. Biol.*, **42**, 623 (2008).
33. M. A. Williams, J. E. Ladbury, Hydrogen bonds in protein-ligand complexes (Protein-ligand interactions), Wiley, 2003.
34. K. Konstantinidis, I. Karakasiliotis, K. Anagnostopoulos, G. C. Boulougouris, *Mol. Syst. Des. Eng.*, **6**, 946 (2021).
35. S. Genheden, U. Ryde, *Expert Opin. Drug Discov.*, **10**, 449 (2015).
36. G. Poli, C. Granchi, F. Rizzolio, T. Tuccinardi, *Molecules*, **25**, 1971 (2020).
37. [T. Simonson, C. Chipot, A. Pohorille, Free energy calculations: Approximate methods for biological macromolecules (Free energy calculations: Theory and applications in chemistry and biology), Springer, Berlin, 2007.
38. V. Acuña-Guzman, M. E. Montoya-Alfaro, L. P. Negrón-Ballarte, C. Solis-Calero, *Pharmaceuticals*, **17**, 750 (2024).
39. L. Bogaard, K. Tsoi, B. van de Steeg, E. F. A. Brandon, L. Geers, M. van Herwaarden, F. Jansman, D. Maas, M. Monster-Simons, D. S. Y. Ong, S. D. Borgsteede, *Front. Pharmacol.*, **15**, 1412692 (2024).
40. F. Lombardo, J. Bentzien, G. Berellini, I. Muegge, *J. Pharm. Sci.*, **110**, 500 (2021).
41. Y. Wei, L. Palazzolo, O. Ben Mariem, D. Bianchi, T. Laurenzi, U. Guerrini, I. Eberini, *Comput. Struct. Biotechnol. J.*, **23**, 3090 (2024).
42. A. C. Severance, P. J. Sandoval, S. H. Wright, *J. Pharmacol. Exp. Ther.*, **362**, 405 (2017).
43. Y. Jing, A. Easter, D. Peters, N. Kim, I. J. Enyedy, *Future Med. Chem.*, **7**, 571 (2015).
44. A. A. Toropov, A. P. Toropova, E. Benfenati, *Toxicol. Mech. Methods*, **30**, 605 (2020).
45. P. Geerlings, *Pharmaceuticals*, **15**, 1112 (2022).
46. Y. Li, M. Lin, M. Tian, G. Ye, X. Zhao, *J. Mol. Liq.*, **390**, 123059 (2023).
47. E. V. Gómez, N. A. Ramírez Guarnizo, J. D. Perea, A. S. López, J. J. Prías-Barragán, *ACS Omega*, **7**, 3872 (2022).
48. R. Pal, P. K. Chattaraj, *J. Comput. Chem.*, **44**, 278 (2023).